RESEARCH ARTICLE

NANO · MICRO small
www.small-journal.com

Stacking Pressure Modulated Deposition and Dissolution of Zinc Anode

*Yuehua Wen, Kesong Yu, Shouren Zhan, Xiaobin Liao, Zhipeng Zhang, Xiaqing Ran, Bowei Li, Suttipong Wannapaiboon, and Mengyu Yan**

Aqueous zinc-ion batteries (ZIBs) are emerging as a promising candidate for large-scale energy storage, offering enhanced safety and low costs. Nevertheless, the disordered growth of zinc dendrites has resulted in low coulombic efficiency and the dangers of short circuits, limiting the commercialization of ZIBs. In this study, a planar growth of zinc along the (002) direction is achieved by regulating the moderate initial stacking pressure during cell cycling and facilitating a larger zinc deposition particle size. The pivotal role of stacking pressure on the zinc nucleation, growth, and dissolution processes is elucidated with in situ pressure X-ray diffraction (XRD), time of flight secondary ion mass spectrometry (TOF-SIMs), and scanning electronic microscopy (SEM). By adjusting the staking pressure from 20 to 300 kPa, the battery cycle time increased 5 times. This work highlights the opportunity to precisely manipulate metal deposition/dissolution with stacking pressure for long-cycle life batteries.

1. Introduction

In recent years, aqueous zinc-ion batteries have emerged as a promising candidate for lead-acid batteries in large-scale energy storage, offering a compelling combination of cost-effectiveness, safety, and environmental compatibility. In comparison to the cost of lead-acid batteries, ~\$260 kWh^{-1}, the lithium-ion batteries with a lithium iron phosphate cathode show a higher cost of \$271 kWh^{-1}. In contrast, aqueous zinc-ion batteries demonstrate compelling economic viability with an estimated material cost of \$192 kWh^{-1}[1–4] significantly lower than conventional lithium-ion batteries. Furthermore, the aqueous zinc-ion battery employs an aqueous solution with a pH of 5 – 7 as the electrolyte.[5,6] Its ionic conductivity is ~1 S cm^{-1}, over ten times higher than the commercialized lithium-ion battery electrolyte.[7–11]

Nevertheless, the growth of zinc dendrites during the Zn deposition and dissolution becomes a significant obstacle to the long-life zinc anodes.[12–15] Furthermore, the hydrogen/oxygen evolution in the electrolyte and the Zn anode corrosion also impact the battery cycle life.[16–20] Researchers spend significant effort on stabilizing the Zn anode, including modifying the electrolyte component,[21–23] constructing the stable solid-electrolyte interface,[24–28] and substrate manipulated Zn anode orientation.[29–32] In the industrial research of lithium-ion batteries, the minimization of interfacial and transport impedance has been achieved by pressurizing the electrode stacks, improving the cycling stability.[33–35] Recent studies have further proved that stacking pressure serves as an effective strategy in improving the metal cell coulombic efficiency and cycle life[36–39] with a tightly stacked metal deposition morphology.[39] However, it is not clear how the stacking pressure affects the deposition and dissolution of zinc metal in aqueous batteries.

In this paper, we designed an in situ pressure-electrochemical coupled X-ray diffraction (XRD) cell. With this in situ cell, we are able to monitor the XRD revolution during cycling and stacking pressure. The results demonstrate that zinc metal can achieve a relatively stable planar growth under suitable pressure (300 kPa), with a cycle life exceeding 100 h in a basic Zn||Ti cell in 1 M $ZnSO_4$ electrolyte. The Zn||VO_2 full cell has an initial capacity of up to 225 mAh g^{-1} and retains 77.3% of its capacity after 100 cycles.

2. Results and Discussion

We used a lab-designed in situ XRD cell with a pressure sensor (**Figure 1a**; Figures S1 and S2, Supporting Information) to precisely control the stacking pressure applied to the cell. Figure 1b illustrates the in situ XRD plot with the corresponding cycling

Y. Wen, K. Yu, S. Zhan, X. Liao, Z. Zhang, X. Ran, B. Li, M. Yan
State Key Laboratory of Advanced Technology for Materials Synthesis and Processing
State Key Laboratory of Silicate Materials for Architectures
School of Materials Science and Engineering
International School of Materials Science and Engineering
Wuhan University of Technology
Wuhan 430070, China
E-mail: ymy@whut.edu.cn

S. Wannapaiboon
Synchrotron Light Research Institute
111 University Avenue
Muang District, Nakhon Ratchasima 30000, Thailand

M. Yan
Zhongyu Feima New Material Technology Innovation Center (Zhengzhou) Co., Ltd.
High Technology Industrial Development Zone
No. 60 Xuelan Road, Zhengzhou 450001, China

The ORCID identification number(s) for the author(s) of this article can be found under https://doi.org/10.1002/smll.202501242

DOI: 10.1002/smll.202501242

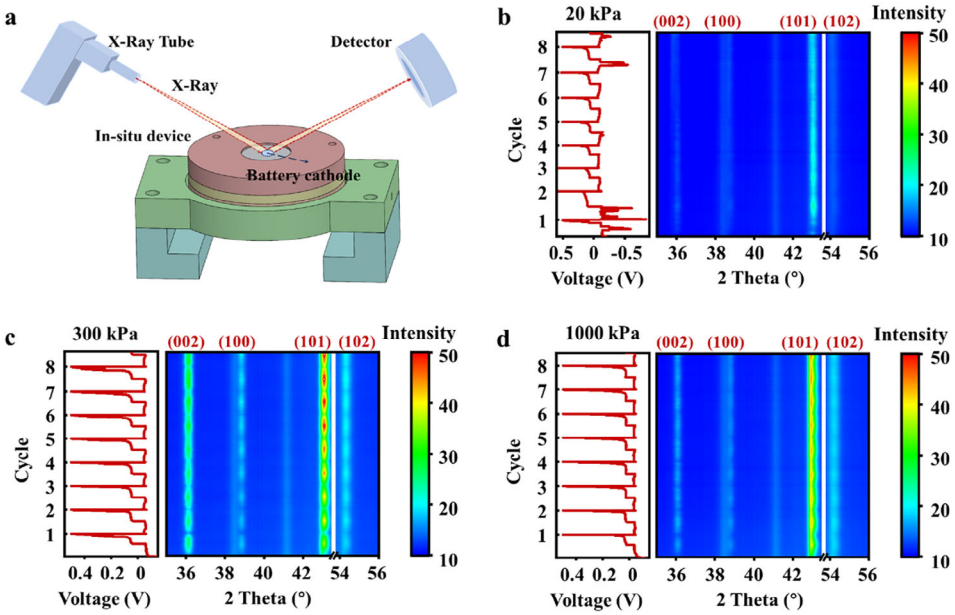

Figure 1. a) Schematic diagram of the in situ pressure-electrochemical coupled XRD device; b–d) The cell cycling curves and in situ XRD profiles of Zn||Ti batteries at 1 mA cm^{-2} and the stacking pressures of 20 kPa (b), 300 kPa (c), 1000 kPa (d).

curve at 20 kPa. In the first two cycles, the contact between the cells is unstable due to the relatively low pressure, leading to a fluctuating voltage. The cycle curve becomes stable starting from the 3rd cycle. The Zn(002), (100), (101), and (102) peaks are visible in the XRD. Among them, the (101) peak gradually increased from 12 to 22 counts, while the other peaks haven't changed significantly. We are unable to capture the deposition and dissolution behavior of Zn metal under 20 kPa. This phenomenon is primarily attributed to inadequate interfacial contact between battery components at the low stacking pressure of 20 kPa, as evidenced by fluctuations in charge/discharge curves and elevated overpotential. At such low-pressure conditions (particularly in localized pressure-deficient regions), Zn deposition manifests disordered and stochastic behavior that does not consistently localize entirely at the cathode side, resulting in simultaneously compromised efficacy of both deposition and dissolution processes. The XRD patterns suggest that some Zn^{2+} are electrodeposited on the cathode but unable to dissolute during the afterward charge.

Figure 1c shows the in situ XRD patterns with the cell cycle at 300 kPa. During the discharge, the Zn (002), (100), (101), and (102) peaks become more obvious, indicating the deposition of anodic Zn. During the following charging, anodic Zn dissolves, making the peak intensity weaker. There exist clear deposition-dissolution processes in the first four discharge-charge cycles, with three distinct gaps between the cycles. It suggests that the dissolution has been processed thoroughly in the first set of several cycles. Meanwhile, the intensity of the Zn peaks increases by cycle. If further increase the stacking pressure to 1000 kPa (Figure 1d), the deposition-dissolution process in situ XRD patterns becomes blurry again, similar to that in 20 kPa. We also observed a much weaker peak intensity for the case of applying 1000 kPa pressure compared to the 300 kPa one. The in situ monitoring of XRD patterns during cycling at other pressures is represented in Figures S3–S6 (Supporting Information)

The peak intensity variation of different crystallite orientations exhibited in Figure 1 is further analyzed. **Figure 2**a–c presents a comparison of the Zn(002), (100), and (101) peak intensities at the pressure of 20, 300, and 1000 kPa. The horizontal axis represents the cycle time, and the vertical axis depicts the peak intensity. In Figure 2c, at 300 kPa, the Zn(002) peak counts increase from 0 to 13.3 in the first discharge and then decrease to 3.4 after charging. In the first 6 cycles, the Zn(002) peak count at the discharged state keeps rising from 13.3 to 18.7 and then levels off from 6 to 8 cycles. The peak count at the charged state is also raised to 11.7, three times to the one observed in the first cycle. The Zn(002) peak at 1000 kPa shows similar trends in the whole 8 cycles, increasing during discharge and decreasing in the charging process. The peak intensity at 1000 kPa, however, is much lower than the intensity at 300 kPa. It increases from 0 to 4.8 during discharge, only 36% compared to the 300 kPa one. The Zn(002) peak intensity doesn't vary significantly in the following cycles. In the 8th cycle, the intensity at the discharge state moves to 6.5. The evolution Zn(002) peak during cycling at 20 kPa is totally different from the ones at 300 and 1000 kPa. Specifically, the peak intensities have no obvious trends between the discharged and charged states. At 20 kPa, the peak counts rise to 2.3 after the first discharge, while the counts are 13.3 at 300 and 4.8 at 1000 kPa. The results show that under this battery system, a moderate stacking pressure of 300 kPa exhibits superior deposition/dissolution performance. This trend also appears in the (002) peak intensity comparison plots at other pressures (Figure S7, Supporting Information).

The Zn(100) and (101) variations during cycling are further investigated, as shown in Figure 2b,c, Figures S8 and S9 (Supporting Information). The trends of Zn(100) and (101) during

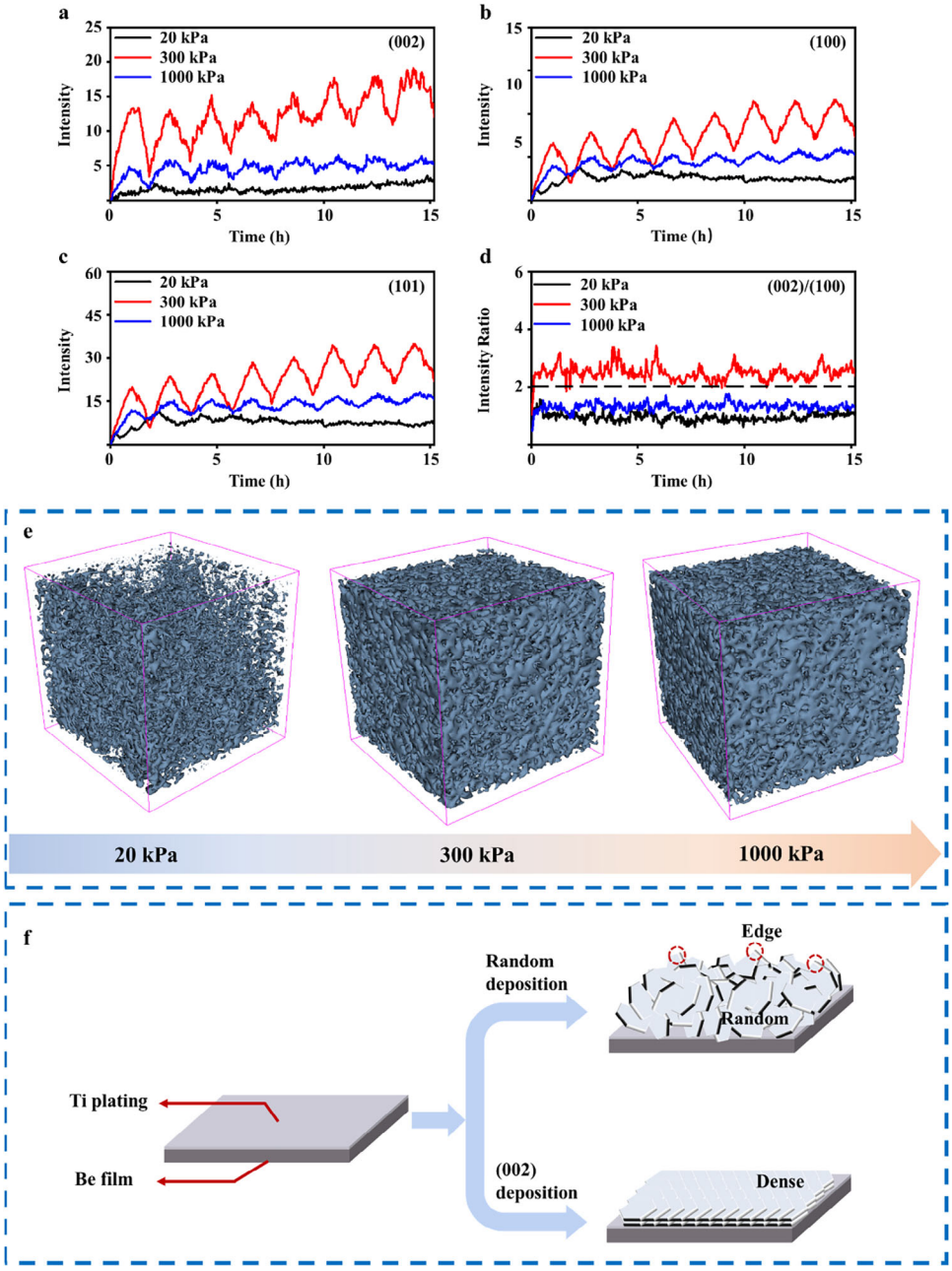

Figure 2. a–c) Comparison of Zn(002) (a), (100) (b) (101) (c) XRD peak intensities on the anodic side at 20, 300, and 1000 kPa; d) The Zn(002)/(100) ratio on the anodic side; e) 3D mapping of TOF-SIMS at 20, 300, 1000 kPa for the 8th cycle deposition. f) Schematic diagram of Zn orientation deposition.

charge/discharge are similar to Zn(002) under all three stacking pressures. It is clear that the peak intensity changes more significantly under 300 kPa than 20 and 1000 kPa. We further investigate the Zn(002)/(100) ratio to have an in-depth understanding of why 300 kPa matters (Figure 2d). The mean ratios are 1.0, 2.5, and 1.2 at 20, 300, and 1000 kPa, respectively. It indicates that there is no obvious crystal orientation during the deposition/dissolution procedure when 20 and 1000 kPa stacking pressures are applied. Interestingly, the 300 kPa pressure is the optimal value, which can induce the Zn crystal deposits along the (002) direction. This confirms that appropriate pressure (300 kPa) effectively promotes preferential growth of Zn metal along the (002) crystal plane. Notably, the crystal structure of zinc is a typical hexagonal close-packed (hcp) structure, consisting of three major crystallographic planes, (002), (101), and (100), with different deposition behavior.[29] Typically, the electro-induced crystallite morphology of zinc exhibits hexagonal flakes due to the minimum surface energy of the (002) plane.[40–43] Therefore, reasonable adjustment of the orientation arrangement of the zinc flakes is beneficial to slow down the dendrite formation. The time of flight secondary ion mass spectrometry (TOF-SIMS) was further employed to investigate the spatial structure of the deposited Zn

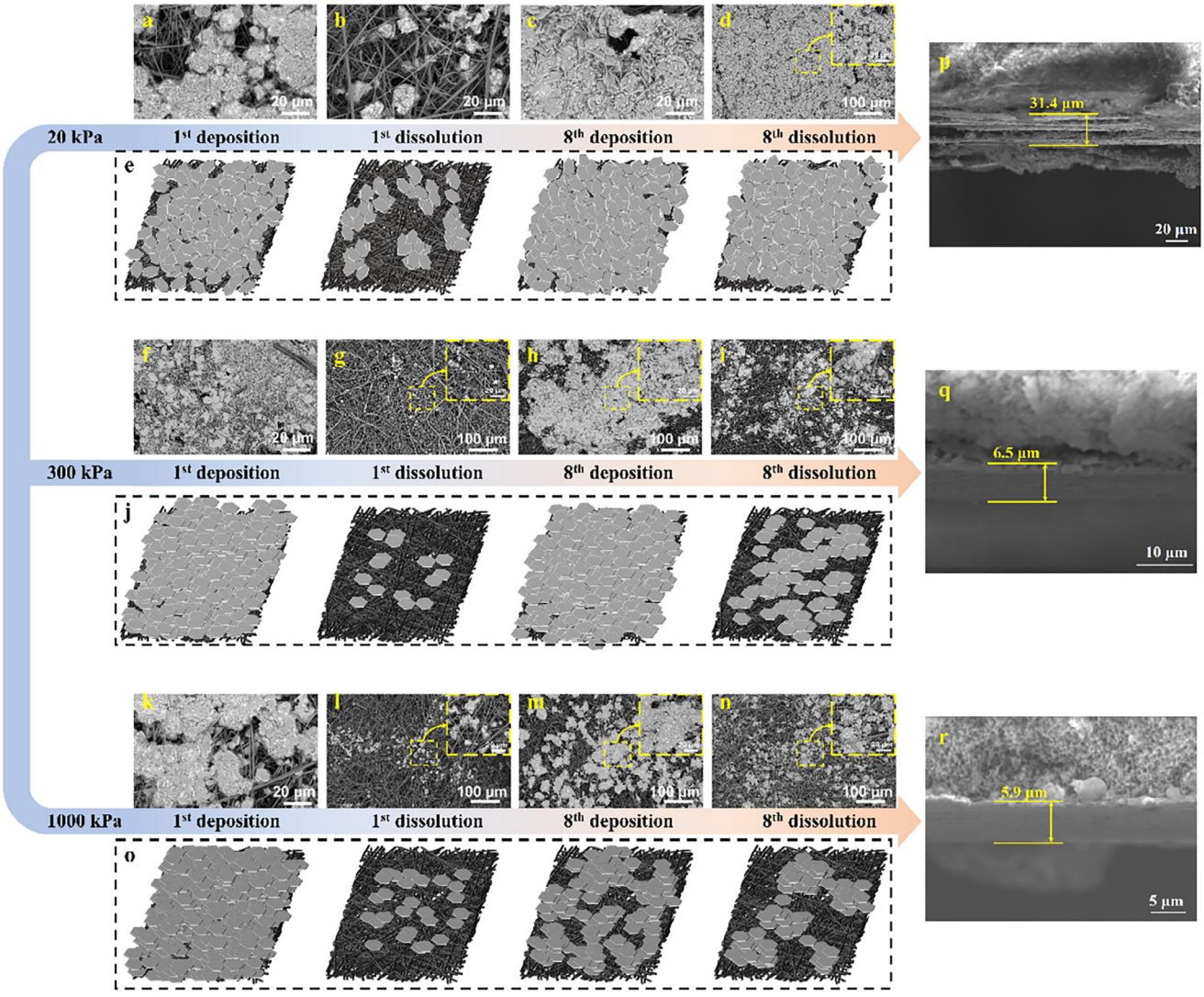

Figure 3. a–o) Deposition/dissolution SEM images and schematic diagrams of Zn||Ti cells cycled at 1 mA cm^{-2} for the 1st and 8th cycles at pressures of 20 kPa (a–e), 300 kPa (f–j), and 1000 kPa (k–o), respectively. p–r) Cross-section SEM images of Zn deposits under pressure of 20 kPa (p), 300 kPa (q), and 1000 kPa (r) after the 8th deposition at 1 mA cm^{-2}.

metal (Figure 2e). It is found that the Zn metal becomes denser by increasing the stacking pressure from 20 to 1000 kPa. The relative density increases from 86% at 20 kPa to 98% at 300 kPa, compared with the density at 1000 kPa. This indicates that the deposition density increases with applied stacking pressure, which aligns with the understanding that stacking pressure affects material density. By combining the TOF-SIMS and in situ XRD results, we are able to plot the schematic diagram at different stacking pressures. (Figure 2f) At relatively low pressure (20 kPa), it could form a loose and scattered structure. Thus, the deposited Zn metal relative density is low and no obvious orientation is observed in the in situ XRD. At the higher pressure (300 kPa), a dense Zn metal layer may form on the Ti electrode with the Zn (002) exposed to the electrolyte, which consequently exhibits the preferred orientation, and results in a higher Zn (002) intensity in XRD. Based on these findings, we achieved controlled preferential growth of deposited Zn along the (002) crystallographic orientation through a simple stacking pressure strategy. However, this hypothesis cannot explain why the crystal orientation was varnished at 1000 kPa.

The scanning electron microscope (SEM) is employed to verify the hypothesis above and investigate the disappeared Zn orientation at 1000 kPa. The batteries with stacking pressure were fully charged/discharged and then disassembled. The separators were collected for the SEM characterization. The preferential adhesion of deposited Zn to the separator over the Ti current collector leads to zinc accumulation on the separator. Crucially, this interfacial selectivity remains non-interferential to SEM-based morphological characterization of Zn deposition patterns. **Figure** 3a–e shows the SEM images and schematic diagrams of the separators after cycled at 20 kPa stacking pressure. It is evident that a large amount of Zn was deposited on the cathode side of the separator at the initial discharging cycle, with limited Zn remaining after the first charge. A substantial amount of deposited hexagonal

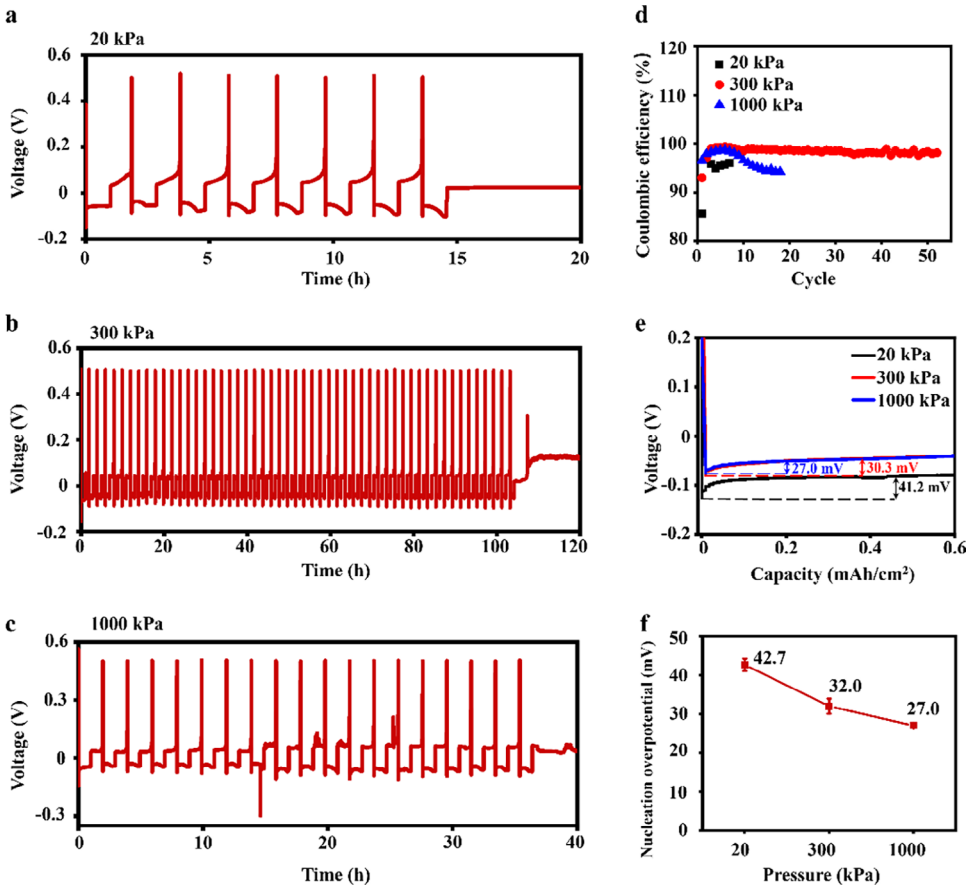

Figure 4. a–c) Cell cycling curves of Zn||Ti cell at 20 kPa (a), 300 kPa (b), and 1000 kPa (c) with 1 M $ZnSO_4$ at 1 mA cm^{-2}; d) Comparison of the cell coulombic efficiencies at 20, 300, and 1000 kPa; e) Nucleation overpotentials at 20, 300, and 1000 kPa; f) The nucleation overpotentials error plots at 20, 300 and 1000 kPa.

zinc was observed at the end of the eighth discharging, exhibiting a highly disordered growth orientation. After the eighth charging, a considerable quantity of Zn remains on the cathode side of the separator. It suggests that a substantial portion of the Zn on the cathode side did not undergo dissolution during the charging process, resulting in the formation of dead Zn. The first cycle SEM images (Figures 3f,g,j) at 300 kPa show a similar morphology to the 20 kPa. After the discharge in the 8th cycle, a large number of hexagonal Zn plates are stacked along the (002) direction, demonstrating a planar growth during the Zn electrodeposition. For the 8th charge, there exists much less residual Zn compared with the 20 kPa sample. Figure 3k–o illustrates the SEM images and their schematic diagrams for the 1st and 8th deposition/dissolution at 1000 kPa. The most significant difference between the 1000 and 300 kPa samples is the morphology at the end of the 8th plating. The 1000 kPa sample shows an island-like morphology with an average particle size of 6.82 µm, smaller than the one obtained at 300 kPa (8.02 µm) (Figure S10, Supporting Information). The ~18% smaller particle size at 1000 kPa hypothesizes a decreased Zn(002)/(100) ratio, as well as the Zn(002) preferred orientation. According to the cross-section SEM images, the thickness of the Zn deposition layer decreases from 31.4 µm at 20 kPa to 6.5 µm at 300 kPa, and it decreases to 5.9 µm when the pressure is further increased to 1000 kPa (Figure 3p–r). It can be clearly seen that at 20 kPa, there is an obvious void layer at the cross-section of the Zn deposition layer, and the dendrites of Zn at the void are random. The observed phenomena stem from pressure-dependent structural evolution: At low stacking pressure (20 kPa), loose Zn deposits progressively form sandwich-like interstitial structures during cycling. At 300 kPa optimal stacking pressure, compact (002)-oriented Zn layers develop with separator elasticity creating protective micro-void interlayers that accommodate volume changes while reducing dendrite penetration risks. However, the 1000 kPa stacking pressure eliminates these critical buffer zones, forcing Zn dendrites into separator pores and accelerating capacity decay. The corresponding energy dispersive spectroscopies show that the deposited layer is Zn (Figures S11–S13, Supporting Information). The above results indicate that the proper pressure increase can help the Zn to deposit densely along the (002) plane, but the further increase in pressure will result in a smaller Zn particle size. This reduced particle size allows deposited Zn to more readily penetrate the separator, inducing battery micro-short circuits (cross-sectional SEM in Figure 3r clearly shows Zn dendrite penetration into the separator), which accounts for the performance decline observed under 1000 kPa pressure in subsequent tests.

The cycling performance was tested with the electrolyte of 1 M $ZnSO_4$ at 1 mA cm^{-2} in a Zn||Ti cell (Figure S14, Supporting

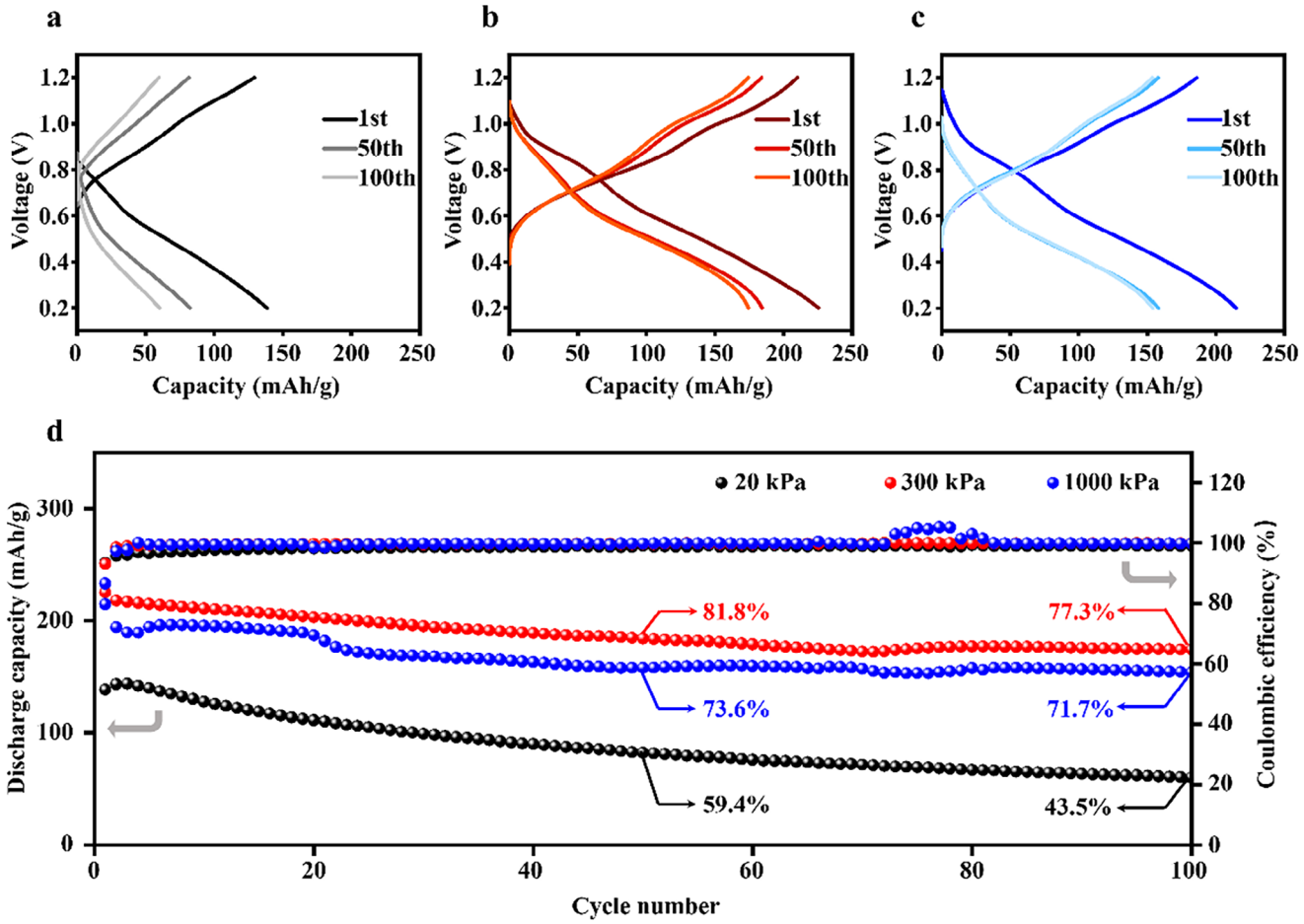

Figure 5. a–c) The charge-discharge curves of Zn||VO_2 cells at 20 kPa (a), 300 kPa, (b) and 1000 kPa (c) with 1 M $ZnSO_4$ at 1 A g^{-1}. d) The cycling performances of the cells at 20, 300, and 1000 kPa.

Information). The cell could cycle 14 h at 20 kPa, followed by a short circuit. (**Figure** 4a) By enhancing the pressure to 300 kPa, the cell cycling capability increased to 104 h. (Figure 4b) At 1000 kPa, the cycled time decreased to 36h. (Figure 4c) Furthermore, the Coulombic efficiency mean value is 98.4% at 300 kPa, while it decreases to 94.4% at 20 kPa and 96.6% at 1000 kPa. (Figure 4d) The relatively high Coulombic efficiency at 300 kPa is attributed to its larger particle size (Figure S10, Supporting Information) and stacked morphology along the Zn (002) direction (Figure 3h). The nucleation overpotentials under three pressures are illustrated in Figure 4e,f. The overpotential is 42.7, 32.0, and 27.0 mV at 20, 300 and 1000 kPa, respectively. The overpotential (η) and nucleation rate (J_n) (Note S1, Supporting Information) obey the following equation,

$$J_n = Ae^{-\frac{\Delta g_n + \eta\varepsilon}{k_B T}} \quad (1)$$

where Δg_n is constant relating to the interfacial free energy and the chemical potential of the crystallizing species, A is a prefactor, k_B is the Boltzmann constant, T is the absolute temperature, and e is the elementary charge. Thus, we are able to calculate the ratio of nucleation rates under different staking pressures with the overpotentials. It is found that the lower overpotential at 1000 kPa leads to the formation of 21% more crystal nuclei than 300 kPa, which is consistent with the ~18% smaller particle size illustrated in Figure S10 (Supporting Information). Thus, we believe that the pressure-dependent variation in nucleation overpotential fundamentally reflects the modulation of Zn deposition nucleation barriers. Under electric field guidance, pressure-regulated nucleation barrier variation results in progressively refined Zn grains with increasing applied pressure.

The Zn||VO_2 batteries were assembled to verify the effect of initial pressure on the full cell (**Figure** 5). Comparing the cycling performance of the Zn||VO_2 full cell at three pressures, we found that at low pressure (20 kPa), its initial capacity is only 138 mAh g^{-1} (Figure 5a), and sharply decreases during cycling, with a capacity retention of 43.5% after 100 cycles. In contrast, the battery at 300 and 1000 kPa shows a higher initial capacity of ~220 mAh g^{-1} (Figure 5b,c), as well as a higher capacity retention of 77.3% and 71.3%, respectively (Figure 5d). The coulombic efficiency (CE) maintains stable proximity to 100% (though the initial 1–2 formation cycles exhibit sub-100% values during activation processes). It is demonstrated that the suitable stacking pressure can not only increase the cycling stability but also the discharge capacity. The comparison of Zn||VO_2 full-cell

performance is shown in Table S1 (Supporting Information). In order to further confirm that the pressure-induced regulation of Zn||VO_2 full-cell performance is independent of the electrolyte, we supplemented the cycling performance of 3 M $Zn(CF_3SO_3)_2$ electrolyte (considered more suitable for aqueous zinc-ion batteries) at 1 A g^{-1} (Figure S15, Supporting Information). The results show that within the first 100 cycles, the battery exhibits a trend similar to that with 1 M $ZnSO_4$. Notably, in subsequent cycles, the battery at 20 kPa stacking pressure shows a significant rapid capacity decrease, while the battery at 1000 kPa stacking pressure develops a micro-short circuit after 166 cycles, with none of them exceeding 200 cycles. This indicates that in full cells, excessively low pressure leads to rapid capacity decrease while excessively high pressure increases the likelihood of short circuits. The in situ synchrotron XRD characterization is further employed to investigate the crystal structure evolution in Zn||VO_2 batteries (Figure S16, Supporting Information). It shows a new diffraction peak at ~4.1°, which is contributed to the $(Zn(OH)_2)_3(ZnSO_4)\cdot 5H_2O$ in the zinc-ion battery. The VO_2(110) at ~13.0° is left shifted during the discharge (correlated to lattice expansion) and recovered after charge. This suggests that the Zn intercalation increases the VO_2 lattice constant.

3. Conclusion

The stacking pressure-dependent Zn deposition and dissolution behavior are investigated by combining in situ pressure XRD, SEM, TOF-SIMS, and electrochemical techniques. The pressure shows an unpredicted effect on the Zn deposition orientation. By increasing the pressure from 20 to 300 kPa, the Zn-deposited morphology changes from a scattered structure to a dense (002) orientated plane. This results in a 5-time longer cycle time in the Zn||Ti cell and a 63% higher capacity in the Zn||VO_2 full battery. It is worth noting that the 300 kPa fits for the Zn deposition, while it may not be the best pressure for the VO_2 cathode. The stacking pressure needs to be adjusted with different electrode materials. This study shines a light on the stacking pressure-modulated orientation deposition and enhanced battery performance.

Supporting Information

Supporting Information is available from the Wiley Online Library or from the author.

Acknowledgements

This work was supported by the National Key Research and Development Program of China (2024YFF0510500), the National Natural Science Foundation of China (52127816, 22409153, and 62305141), the Key Research and Development Program of Hubei Province (2022BAA027), and the Postdoctoral Fellowship Program of CPSF under Grant Number GZC20232013. The authors would like to acknowledge the Synchrotron Light Research Institute (Public Organization), SLRI, for the provision of beamtime and the staff of beamline 7.2 W for their assistance. The authors also would like to acknowledge the support of EVASTAR co. for in situ XRD measurement.

Conflict of Interest

The authors declare no conflict of interest.

Data Availability Statement

The data that support the findings of this study are available from the corresponding author upon reasonable request.

Keywords

deposition/dissolution, stacking pressure, zinc anode, zinc-ion batteries

Received: January 30, 2025
Revised: March 4, 2025
Published online: March 11, 2025

[1] K. Mongird, V. V. Viswanathan, P. Balducci, J. Alam, V. Fotedar, V. Koritarov, B. Hadjerioua, "Energy Storage Technology and Cost Characterization Report", **2019**.
[2] P. P. Lopes, V. R. Stamenkovic, *Science* **2020**, *369*, 923.
[3] W. He, W. Guo, H. Wu, L. Lin, Q. Liu, X. Han, Q. Xie, P. Liu, H. Zheng, L. Wang, X. Yu, D.-L. Peng, *Adv. Mater.* **2021**, *33*, 2005937.
[4] H. Dong, J. Li, J. Guo, F. Lai, F. Zhao, Y. Jiao, D. J. L. Brett, T. Liu, G. He, I. P. Parkin, *Adv. Mater.* **2021**, *33*, 2007548.
[5] Y. Wang, T. Wang, S. Bu, J. Zhu, Y. Wang, R. Zhang, H. Hong, W. Zhang, J. Fan, C. Zhi, *Nat. Commun.* **2023**, *14*, 1828.
[6] T. Peng, Y. Xing, L. Mu, C. Wang, N. Zhao, W. Liao, J. Li, G. Zhao, *Chin. Chem. Lett.* **2024**, 110039.
[7] M. Winter, R. J. Brodd, *Chem. Rev.* **2004**, *104*, 4245.
[8] X. Xie, S. Liang, J. Gao, S. Guo, J. Guo, C. Wang, G. Xu, X. Wu, G. Chen, J. Zhou, *Energy Environ. Sci.* **2020**, *13*, 503.
[9] C. Li, X. Shi, S. Liang, X. Ma, M. Han, X. Wu, J. Zhou, *Chem. Eng. J.* **2020**, *379*, 122248.
[10] S. Guo, S. Liang, B. Zhang, G. Fang, D. Ma, J. Zhou, *ACS Nano* **2019**, *13*, 13456;
[11] C.-X. Zhao, J.-N. Liu, B.-Q. Li, D. Ren, X. Chen, J. Yu, Q. Zhang, *Adv. Funct. Mater.* **2020**, *30*, 2003619.
[12] W. Zhang, Q. Zhao, Y. Hou, Z. Shen, L. Fan, S. Zhou, Y. Lu, L. A. Archer, *Sci. Adv.* **2021**, *7*, eabl3752.
[13] Y. Zuo, K. Wang, P. Pei, M. Wei, X. Liu, Y. Xiao, P. Zhang, *Mater. Today Energy* **2021**, *20*, 100692.
[14] H. Dai, T. Sun, J. Zhou, J. Wang, Z. Chen, G. Zhang, S. Sun, *Nat. Commun.* **2024**, *15*, 8577.
[15] H. Tian, J. Yang, Y. Deng, W. Tang, R. Liu, C. Xu, P. Han, H. Fan, *Adv. Energy Mater.* **2022**, *13*, 2202603.
[16] M. Li, Z. Li, X. Wang, J. Meng, X. Liu, B. Wu, C. Han, L. Mai, *Energy Environ. Sci.* **2021**, *14*, 3796.
[17] Y. Zhao, Z. Chen, X. Gao, H. Dong, X. Zhao, G. He, H. Yang, *Angew. Chem., Int. Ed.* **2024**, *64*, 202415251.
[18] Q. Nian, X. Luo, D. Ruan, Y. Li, B.-Q. Xiong, Z. Cui, Z. Wang, Q. Dong, J. Fan, J. Jiang, J. Ma, Z. Ma, D. Wang, X. Ren, *Nat. Commun.* **2024**, *15*, 4303.
[19] Y. Qian, L. Chen, *J. Energy Chem.* **2024**, *99*, 553.
[20] T. Zhang, J. Ju, Z. Zhang, D. Su, Y. Wang, W. Kang, *J. Energy Chem.* **2024**, *98*, 562.
[21] P. Sun, L. Ma, W. Zhou, M. Qiu, Z. Wang, D. Chao, W. Mai, *Angew. Chem., Int. Ed.* **2021**, *60*, 18247.
[22] Q. Zhang, Y. Ma, Y. Lu, Y. Ni, L. Lin, Z. Hao, Z. Yan, Q. Zhao, J. Chen, *J. Am. Chem. Soc.* **2022**, *144*, 18435.
[23] R. Qi, W. Tang, Y. Shi, K. Teng, Y. Deng, L. Zhang, J. Zhang, R. Liu, *Adv. Funct. Mater.* **2023**, *16*, 2306052.
[24] Z. Guo, L. Fan, C. Zhao, A. Chen, N. Liu, Y. Zhang, N. Zhang, *Adv. Mater.* **2022**, *34*, 2105133.

[25] Z. Zhao, R. Wang, C. Peng, W. Chen, T. Wu, B. Hu, W. Weng, Y. Yao, J. Zeng, Z. Chen, P. Liu, Y. Liu, G. Li, J. Guo, H. Lu, Z. Guo, *Nat. Commun.* **2021**, *12*, 6606.
[26] H. Yin, H. Wu, Y. Yang, S. Yao, P. Han, Y. Shi, R. Liu, *Small* **2024**, *20*, 2404367.
[27] H. Wu, H. Yin, H. Tian, J. Yang, R. Liu, *Energy Environ. Mater.* **2024**, *8*, e12839.
[28] Z. Yao, W. Zhang, J. Zhu, *J. Energy Chem.* **2024**, *96*, 359.
[29] Y. Zou, X. Yang, L. Shen, Y. Su, Z. Chen, X. Gao, J. Zhou, J. Sun, *Energy Environ. Sci.* **2022**, *15*, 5017.
[30] Y. Zhang, X. Han, R. Liu, Z. Yang, S. Zhang, Y. Zhang, H. Wang, Y. Cao, A. Chen, J. Sun, *Small* **2022**, *18*, 2105978.
[31] W. Yuan, X. Nie, G. Ma, M. Liu, Y. Wang, S. Shen, N. Zhang, *Angew. Chem., Int. Ed.* **2023**, *62*, 202218386.
[32] Z. Liu, Z. Guo, L. Fan, C. Zhao, A. Chen, M. Wang, M. Li, X. Lu, J. Zhang, Zhang, Y.u, N. Zhang, *Adv. Mater.* **2024**, *36*, 2305988.
[33] T. Hirai, I. Yoshimatsu, J. i. Yamaki, *J. Electrochem. Soc.* **1994**, *141*, 611.
[34] T. Wulandari, D. Fawcett, S. B. Majumder, G. E. J. Poinern, *Battery Energy* **2023**, *2*, 20230030.
[35] F. Chen, T. Chen, Z. Wu, X. Kong, X. Meng, X. Han, L. Lu, Y. Zheng, M. Ouyang, *J. Power Sources* **2024**, *610*, 234717.
[36] C. Fang, B. Lu, G. Pawar, M. Zhang, D. Cheng, S. Chen, M. Ceja, J.-M. Doux, H. Musrock, M. Cai, B. Liaw, Y. S. Meng, *Nat. Energy* **2021**, *6*, 987.
[37] A. J. Louli, M. Genovese, R. Weber, S. G. Hames, E. R. Logan, J. R. Dahn, *J. Electrochem. Soc.* **2019**, *166*, A1291.
[38] R. Weber, M. Genovese, A. J. Louli, S. Hames, C. Martin, I. G. Hill, J. R. Dahn, *Nat. Energy* **2019**, *4*, 683.
[39] X. Yin, W. Tang, I. D. Jung, K. C. Phua, S. Adams, S. W. Lee, G. W. J. N. E. Zheng, *Nano Energy* **2018**, *50*, 659.
[40] T. Wang, J. Sun, Y. Hua, B. N. V. Krishna, Q. Xi, W. Ai, J. S. Yu, *Energy Storage Mater.* **2022**, *53*, 273.
[41] X. Wang, J. Meng, X. Lin, Y. Yang, S. Zhou, Y. Wang, A. Pan, *Adv. Funct. Mater.* **2021**, *31*, 2106114.
[42] X. Jia, C. Liu, Z. G. Neale, J. Yang, G. Cao, *Chem. Rev.* **2020**, *120*, 7795.
[43] H. Fu, L. Xiong, W. Han, M. Wang, Y. J. Kim, X. Li, W. Yang, G. Liu, *Energy Storage Mater.* **2022**, *51*, 550.